UKAEA FUS 540

EURATOM/UKAEA Fusion

Some topological properties of plasma equilibria

J.P. Christiansen

January 2007

EURATOM/UKAEA Fusion Association

Culham Science Centre
Abingdon
Oxfordshire
OX14 3DB
United Kingdom

Telephone: +44 1235 820220
Facsimile: +44 1235 466435

UKAEA

SOME TOPOLOGICAL PROPERTIES OF PLASMA EQUILIBRIA

J P CHRISTIANSEN

EURATOM/UKAEA Fusion Association
Culham Science Centre
Abingdon, Oxon OX14 3DB, UK

Abstract

Some properties of axisymmetric equilibrium solutions for the poloidal flux function $\psi(R, Z)$ in toroidal geometry are examined, where ψ is a solution to the non-linear Grad-Shafranov equation whose right hand side features two unknown functions $p'(\psi)$ and $f'(\psi)$; p is plasma pressure, f is toroidal R times toroidal field, while the prime denotes differentiation w.r.t. ψ. A brief review is given of previous work on analytic methods developed to find solutions ψ from analytic representations of (p, f). The review includes numerical methods to find ψ from experimental data on ψ and/or $\nabla\psi$ along curves outside the plasma. The latter, referred to as equilibrium reconstruction, assumes that the functional forms of (p, f) are given. Equilibrium reconstruction has formed the basis of data analysis on tokamak experiments like JET, TFTR, DIII-D, JT60 and ASDEX. Studies have been made to examine if it is possible to find solutions ψ from the knowledge of ψ and $\nabla\psi$ on some contour embracing the plasma cross section, but without making prior assumptions about (p, f). This study has involved many attempts to relate in general the functions (p, f) to the topological properties of the curves of constant ψ and constant χ, where χ is the function orthogonal to ψ in the poloidal plane. Previous work has shown that (p, f) can be determined if the full geometry of the ψ curves alone is known. It is emphasized that this equilibrium reconstruction study is still inconclusive. An analytical equilibrium solution (Solovev) has been used as an example in our study and many of its properties are outlined. The equilibrium topology uniquely determines the functional variation of the cross field guiding centre drift motion, which in turn determines the neoclassical thermal flux. It is shown that this drift motion is at a maximum close to the locus of inflexion points of the χ curves, i.e. along a curve connecting points where the curvature of the χ curves is zero.

1 Introduction

1.1 Overview and motivation for the study

The reviews by Morozov & Solovev [1] and by Solovev & Shafranov [2] describe many general properties of plasma equilibria e.g. magnetic field lines, magnetic field strength and topology for non-axisymmetric and axisymmetric equilibria. We shall consider only tokamak equilibria which exhibit toroidal axisymmetry as decsribed in subsection 1.2. Any axisymmetric toroidal equilibrium is expressed by a function $\psi(R,Z)$ for the poloidal flux. In subsection 1.3 we make the distinction between three categories of equilibria and show how these relate to analytic solutions and solutions derived from experimental data. The latter is known as equilibrium reconstruction and subsections 1.4 - 1.6 review a variety of methods developed during the last 35 years. Two examples of analytic solutions are briefly given in section 2. The Solovev equilibrium solution [3] used in many applications is described in section 3. Section 4 presents various formulae for the topology of the equilibrium. We have used these formulae in attempts to relate generic properties of the equilibrium topology to the current distribution. Our study originates from the early work on equilibrium reconstruction [4] which established the link between the topology of the flux surfaces and the toroidal current distribution. The problem investigated in this paper is whether the current distribution can be determined solely from experimental data external to the plasma, i.e. with no information about the topology of the internal flux surfaces; the current distribution is specified by two functions $(p(\psi), f(\psi))$ of just one variable ψ (see next subsection). A solution to this problem, if it exists, would have a major impact on analysis of tokamak data. It would also have an impact in astro-physics, especially on attempts to determine the mass distribution of the sun, assuming that this distribution is not spherically symmetric. In mathematics the problem is known as the Cauchy problem as described in section 5: can two one-dimensional functions (p,f) be determined from two different one-dimensional functions $\psi(\ell)$ and $\nabla\psi(\ell)$ on some curve Γ external to the plasma, where ℓ denotes the arc length along Γ. Thus in this problem both Dirichlet and Neuman boundary conditions are imposed . After numerous attempts to solve this problem we emphasize that *the problem remains unresolved.* The topology also determines the guiding centre drift motion which in turn together with collisions determines the neoclassical heat flux. Section 6 gives formulae for the guiding centre velocities. The computations in section 6 on that component orthogonal to the ψ surfaces show "a drift loss cone", a banana shaped region in which the drift velocity, and hence the heat flux, is at a maximum. The conclusion to an unresolved problem is the subject of continued research on that problem.

1.2 (R,ϕ,Z) and (ψ,ϕ,χ) coordinates

We shall here consider only axis-symmetric solutions appropriate for tokamak equilibria. Such equilibria are solutions to the Grad-Shafranov equation [5, 6, 7] which links the poloidal flux function ψ to the toroidal current density J_ϕ in toroidal geometry (R,ϕ,Z). We shall occasionally use cylinder geometry (R,θ,Z) where B_Z, J_Z denote the longitudinal field,

current density. The equilibrium equation in cylindrical and toroidal geometry is

$$\nabla^2\psi = \frac{\partial^2\psi}{\partial R^2} + \frac{\partial^2\psi}{\partial Z^2} = -\mu_0 J_Z(\psi) = -\frac{d}{d\psi}(p + B_Z^2/2\mu_0)$$
$$\Delta_*\psi = \frac{\partial^2\psi}{\partial R^2} - \frac{1}{R}\frac{\partial\psi}{\partial R} + \frac{\partial^2\psi}{\partial Z^2} = -\mu_0 R J_\phi = -\mu_0 R^2\frac{dp}{d\psi} - f\frac{df}{d\psi} \qquad (1)$$

In Eq.(1) $p = p(\psi)$ is the plasma pressure and $f = f(\psi) = RB_\phi$, toroidal R times toroidal field; often the RHS terms are denoted by p' and ff'. Solutions $\psi(R, Z)$ can be found within a domain Ω in (R, Z) whose boundary is Γ; in some cases of analytic representations, Ω may be infinite. Boundary conditions like $\psi\,|_\Gamma$ (Dirichlet type) or $\nabla\psi\,|_\Gamma$ (Neuman) may be specified. In the next subsections we shall see that there exist various categories of solutions depending on how the problem is posed. Solutions to Eq.(1) are functions involving two types of basis functions

$$\psi_+ = \sum_{mn} \alpha_{mn}\,\psi_{mn}(R^{2m}, Z^{2n}) \;,\; \psi_- = \sum_{mn} \beta_{mn}\,\psi_{mn}(R^{2m}, Z^n) \qquad (2)$$

The even-even power basis functions yield up-down symmetric solutions $\psi_+(R, Z) = \psi_+(R, -Z)$; similarly the even-odd power basis functions produce anti-symmetric solutions $\psi_-(R, Z) \neq \psi_-(R, -Z)$ [8]. These simple basis functions of Eq.(2) result from a separation of the variables (R, Z) followed by subsequent expansions of the Z function like $e^{\pm\lambda Z}$ and the R function. The latter can be Bessel functions [9], Coulomb wave functions [10] or more complex polynomials [11]. The cited references have all assumed functional dependences $p(\psi), f(\psi)$ which result in forms of Eq.(1) that are linear in ψ.
We have also studied a function $\chi(R, Z)$ which describes the curves orthogonal to the flux surfaces $\psi(R, Z)$. These curves of constant χ represent the projected paths of guiding centre drifts across the plasma surfaces. Once a solution $\psi(R, Z)$ is known, then a solution $\chi(R, Z)$ can in theory be found from the orthogonality relation

$$\nabla\psi \cdot \nabla\chi = 0 \;,\; \nabla\chi = \xi^{-1}(R, Z)\,(-\frac{\partial\psi}{\partial Z}, \frac{\partial\psi}{\partial R}) \qquad (3)$$

The function $\xi(R, Z)$ can be any continous function; the appearance of ξ as ξ^{-1} is due to convention (see subsections 3.5 & 4.1). A computational model for the construction of discrete orthogonal coordinates $\chi_i(R_j, Z_j)$ from a set of discrete points $\psi_i(R_j, Z_j)$ has been developed by Barfield [12] and Potter & Tuttle [13]; subscripts i refer to curves of constant χ and ψ respectively. The approximation made in [13] is to assume that ξ can be expressed in the product form $\xi = q_1(R)q_2(Z)$ within a computational cell and then ξ has a discontinous jump at a cell boundary. This decomposition is a better approximation than the original one made by Barfield [12] who simply assumed constant ξ in a computational cell. A parametric solution for the orthogonal coordinate χ can also in principle be found from the following differential equation in which superscript χ indicates that χ is constant

$$(\frac{\partial Z}{\partial R})^\chi = -(\frac{\partial\psi}{\partial R})(\frac{\partial\psi}{\partial Z})^{-1} \qquad (4)$$

Equation(4) is usually a highly non-linear differential equation for curves $Z(R, \chi = \chi_1)$, e.g. many solutions $\psi(R, Z)$ involve terms like Z^{2n} (see Eq.34). In section 2 we shall consider some analytic solutions to Eq.(1). With these it is convenient to use a non-dimensional flux

surface label x defined via a dimensionless function $s(x)$ which describes the geometry, i.e. shape $x(R,Z)$ of the flux surfaces, usually $s(x) = x^{2m}$. Ampere's law gives via integration around the plasma boundary Γ_b

$$\psi \;=\; \psi_0\; s(x)\;,\;\; \oint \frac{\psi_0}{R} \mid \nabla s(x) \mid d\ell \;=\; \mu_0\; I_\phi \;\Rightarrow\; \psi_0 \;=\; \mu_0\; R_0\; I_\phi \left[\oint \frac{R_0}{R} \mid \nabla s(x) \mid d\ell\right]^{-1} \quad (5)$$

where I_ϕ is the total plasma current and R_0 is the R coordinate for the magnetic axis location (R_0, Z_0), i.e. major radius; minor radius is a; the integral in brackets is a dimensionless number which according to [4] depends only on the shape parameters for the boundary, e.g. ellipticity κ, triangularity δ as well as the inverse aspect ratio $\epsilon = a/R_0$. Solutions to Eq.(1) are often presented graphically as a set of flux surfaces, Such graphs show visually the radial variations of the key equilibrium shape functions: i) Shafranov shift, $\Delta(x)$, ii) elongation, $\kappa(x)$, iii) triangularity, $\delta(x)$, iv) single or double null separatrix. A knowledge of two of these three profiles is sufficient to determine the entire current distribution, J_ϕ [4]. The definitions of the shape parameters have been subject to variations in the past 35 years; however, we shall use those definitions adopted when the international tokamak confinement database was established [14]. We return to this in section 4.

1.3 Equilibrium categories

Properties of equilibrium solutions $\psi(R,Z)$ and how to obtain the latter are reviewed by Lackner [15] who discusses computational problems together with the problem of determining the plasma boundary Γ_b. Reference [15] also describes convergence criteria while reference [16] discusses the non-uniqueness of equilibria; reference [4] explains the link between flux surface geometry and current density. The computational models have been reviewed by McNamara [17]. In general we can divide equilibrium solutions into three categories which feature dimensional constants ψ_0, P_0 and F_0 in units [Vs], [Jm^{-3}], [Vsm^{-1}] respectively and a set of dimensionless parameters $(p_j, f_j, \Pi_j, \Phi_j)$. These constants and parameters together characterize the functions p' and ff' on the RHS of Eq.(1).

Category I has analytically known solutions, usually found with the following simple functions on the RHS of Eq.(1) which allow for a constant term and a term linear in $\psi \sim x^{2m}$

$$\frac{dp}{d\psi} \;=\; \frac{P_0}{\psi_0}\;(p_1 \;+\; p_2\; x^{2m})\;,\;\; f(\psi)\frac{df}{d\psi} \;=\; \frac{F_0^2}{\psi_0}\;(f_1 \;+\; f_2\; x^{2m}) \quad (6)$$

The domain Ω is infinite, but a plasma boundary $\Gamma_b(P_L)$ can be determined where P_L denotes the location of some point on a plasma limiter. Alternatively Γ_b may be a separatrix which can be determined from the analytic representation of ψ. Some solutions with $p_2 = 0, f_2 = 0$ will be described in section 2.

Category II has computed solutions with non-trivial functions on the RHS of Eq.(1), e.g. functions which lead to forms of Eq.(1) that are non-linear

$$\frac{dp}{d\psi} \;=\; \frac{P_0}{\psi_0} \sum_{j=0}^{J1} p_j\; x^j\;,\;\; f(\psi)\frac{df}{d\psi} \;=\; \frac{F_0^2}{\psi_0} \sum_{j=0}^{J2} f_j\; x^j \quad (7)$$

Equation(7) can be considered a generalisation of Eq.(6) and it requires a numerical method to compute ψ; the dimensional constants P_0, F_0, ψ_0 are given. In category II the plasma boundary must be given either in an analytic form or as a set of pre-computed points $\Gamma_b(R_k, Z_k), k = 1, K$, since the computation takes place on a finite grid. The next subsection will discuss various computations.

Category III equilibria are reconstructed from magnetic data and sometimes constrained by additional data. A fast method approximates J_ϕ by a filaments or wires (see section 1.4). For complete equlibrium reconstruction a variety of functions on the RHS of Eq.(1) have been tried, e.g basis functions different from polynomials

$$\frac{dp}{d\psi} = \frac{P_0}{\psi_0} \sum_{j=0}^{J1} p_j \, e^{\pi_j x} \; , \; f(\psi)\frac{df}{d\psi} = \frac{F_0^2}{\psi_0} \sum_{j=1}^{J2} f_j \, \cos(\phi_j x) \tag{8}$$

A part of the reconstruction problem is to determine the shape of Γ_b from one of two conditions: either it is determined as a ψ contour passing through a limiter point P_L or it is determined as a separatrix with one or two x-points. This determination takes place within the "inner iteration cycle". In the "outer iteration cycle" the parameter set $(p_j, \pi_j, f_j, \phi_j)$ are varied until some convergence criteria is satisfied. The dimensional constants P_0, F_0 may also be varied. Only the total plasma current $I_\phi \sim \psi_0/(\mu_0 R_0)$ (Eq.5) is given. In some cases the use of a particular form for p', ff' like those of Eqs.(6-8) may be incompatible with the given data and no solution can be found. Experience from the analysis of JET data shows that such situations can arise at the beginning of the current rise phase or a short time interval before a major MHD event, sawtooth crash, external kink or disruption, i.e. the magnetic data is incompatible with the assumption of axisymmetry, such that Eq.(1) does not apply.

1.4 Equilibrium computation

Early tokamak equilibrium calculations were limited by finite computing resources unlike today. The solution $\psi(R, Z)$ could be evaluated on a grid as small as 15 by 30 points. The major fusion laboratories each had an equilibrium code. At Oak Ridge National Laboratory (ORNL) the code by Callen & Dory [18] was restricted to solve circular equilibria, i. e. it essentially calculates the Shafranov shift Δ for each surface. The Culham Laboratory equilibrium code POTENT [19] was used extensively for equilibrium and stability calculations. An extension to three dimensional non-axisymmeteric equilibria was made to study the influence from the iron core on the JET tokamak. The IPP Garching code by Feneberg & Lackner [20] used the simple expressions of Eq.(6) together with multi-coil specifications. The Kurchatov Institute code by Zakharov [21] embodied "the virtual casing principle" to compute equilibria with complex coil configurations, but with a simple form of the RHS of Eq.(1) like Eq.(6). At Gulf General Atomic (GA) the code by Chu et al. [22] was used to compute the highly elongated Doublet II equilibria. Around 1980 a new computationally fast, but non-exact method was developed by Lao, Hirshman and Wieland [23]. The approximation made in this work is to find moment solutions to Eqs.(1). This can

be implemented computationally if each plasma surface is expressed as

$$R(x,\zeta) \;=\; \sum_{m=0}^{M_R} R_m(x)cos(m\zeta)\;,\; Z(x,\zeta) \;=\; E(x)\;\sum_{m=1}^{M_Z} Z_m(x)sin(m\zeta) \qquad (9)$$

In Eq.(9) the moments (R_m, Z_m) depend on the flux surface label. $R_0(x=0)$ is the magnetic axis location and $E(x)$ is approximately the elongation κ of surface x. The angle parameter ζ is related to the poloidal angle θ via the transformation

$$\zeta \;=\; \theta \;+\; \lambda\,\sin\theta\;,\;\; |\,\lambda\,| \;<\; 1 \qquad (10)$$

This formalism is embodied in the VMOMS code [24] - [25] and in various codes interpreting soft x-ray data such as the one on JET. The representation is particularly useful for 1 1/2 D transport calculations such as the interpretative calculations of the TRANSP code [26, 27]. The formalism in Eq.(9) can be extended to 3D non-axisymmetric equilibria [28] by replacing $m\zeta$ by $m\zeta - n\phi$. One shortcoming of the moment representation Eq.(9) is that it cannot deal with x-point separatrix contours. Thus the 1 1/2 D predictive calculations of the JETTO code at JET [29, 30] use a conventional equilibrium solver ESCO [31] which is similar to POTENT. Similarly the TRANSP code has replaced the representation of Eq.(9) by that of EFIT [32] (see subsection 1.6) as standard JET equilibria now feature a separatrix.

1.5 Fast equilibrium reconstruction

The equilibrium reconstruction techniques start from the work by Shafranov [33] which demonstrates how the global equilibrium parameter $\Lambda \;=\; \beta_I + 1/2\ell_i$, the sum of plasma beta and internal inductance, can be determined from external magnetic measurements. Various methods to identify the plasma bounday shape from one tokamak discharge before the next one (intershot analysis) have been embodied in the so-called "fast boundary solvers": the method by Swain et al. [34] used the approximation for data from ISX at ORNL

$$J_\phi \;=\; \sum_{j=1}^{J} I_j\;\delta(R-R_j)\delta(Z-Z_j)\;,\; \boldsymbol{I}_{wire} \;=\; (I_1, I_2, ...I_J) \qquad (11)$$

The continuous plasma current distribution is represented by a number of current carrying wires. Equation(11) can be generalised from current carrying wires (i.e. points) to a current carrying cylinder (curve in (R,Z) space) as in the method by Feneberg & Lackner [35]; this latter method was used in the JET intershot analysis code FAST [36]. When internal divertor coils were fitted to JET a new numerical method based on vacuum solutions was introduced [37]; this method is so fast that it runs real-time displays of the evolving plasma boundary. The GA code MFIT [32] has used a simplified parametric representation replacing Eq.(8). This code has developed into EFIT, which is in use at several fusion laboratories. At JET a different version EFITJ [38] has been developed and at Culham this has been further developed into [39] (see next subsection). In fast equilibrium construction codes the poloidal magnetic field $\boldsymbol{B}_{pol}$ and poloidal flux $\boldsymbol{\psi}$ are written as vectors expressing the values of the magnetic field $B_i, (i=1,I)$, and poloidal flux $\psi_k, (k=1,K)$, at respectively the I and K

spatial locations, where the measurements are made. The speed advantage of fast solvers lies in the following representations

$$\boldsymbol{B}_{pol} = \underline{\underline{\mathcal{B}}} \cdot \boldsymbol{I}_{wire} \ , \ \psi = \underline{\underline{\Psi}} \cdot \boldsymbol{I}_{wire} \tag{12}$$

The two matrices $\underline{\underline{\mathcal{B}}}$ and $\underline{\underline{\Psi}}$ are precalculated only once for a given set of wire coordinates (R_j, Z_j). Evaluation of the vectors in Eq.(12) $\boldsymbol{B}$ and $\boldsymbol{\psi}$ thus involves only $2J$ multiplications for any point (R, Z) inside the precalculated space. The solution $\boldsymbol{I}_{wire}$ is itself found from a χ^2 fit to external magnetic data. This involves the inversion of a J by J matrix.

1.6 Complete equilibrium reconstruction

The equilibrium reconstruction codes began when tokamaks like JET, DIII-D, JT-60 had magnetic diagnostics installed precisely for the purpose of equilibrium reconstruction. On JET such data would include: i) measurements of poloidal flux ψ by flux loops along the outer vessel surface; ii) measurements of the poloidal field B_{pol} by pick-up coils placed along the inner vessel surface; iii) measurements of the diamagnetic flux $\Delta\Phi$; iv) currents in poloidal-toroidal field coils. DIII-D and JT-60 would produce similar data.
At CEA Fontenay and later at Cadarache the IDENTB code [40] was developed under a JET contract. It was later replaced by the IDENTC and IDENTD versions [41]. The IDENTB,C,D codes featured a finite element representation of the toroidal current density J_ϕ; each version had a higher order element than its predecessor. These codes also featured a computational grid generator which could adapt itself to a variety of JET scenarios. IDENTB,C used the exponential terms in Eq.(8) while IDENTD used Eq.(7). To obtain a new solution ψ^i at iteration i in the inner cycle, the external field produced by poloidal field coils was reproduced computationally from a current distribution I_{ves} flowing on the JET vessel surface just as in the original FAST code [35]. When the JET internal divertor coils were fitted to JET, IDENTD was replaced by a new version of EFIT.
At GA the EFIT code [32], which would later develop into the EFITJ code [38], was developed with a fixed square grid uniform in (R, Z) which for JET would cover the entire region inside the iron core. EFIT uses Eq.(7) and employs a finite difference formulation of Eq.(1). The code has been used extensively in the fusion community and its solutions ψ are used in TRANSP transport calculations. A fast and simplified version of EFIT produces data between JET pulses (intershot analysis). A more special version of EFIT has used Thomson scattering data on p, polarimeter data on $\int B_{pol} d\ell$ and MSE data on B_{pol} to constrain the solutions [39].

2 Analytic equilibrium solutions

We consider a few solutions which are represented by compact analytic expressions, i.e. not by infinite series. The solutions which we consider, are idealised equilibria because the RHS terms of Eq.(1) are either constant or linear (Eq.6) unlike experimentally determined equilibria, which normally have the RHS terms peaked on axis $x = 0$ and then falling of with

increasing x; in many cases the current density at the boundary $J_\phi(R, x = x_b) = 0$. We can divide analytic solutions into three classes: i) approximate solutions using local expansions near x-points or global expansions in the inverse aspect ratio $\epsilon = a/R_0$; ii) compact functions for ψ that are easy and fast to compute, i.e. they involve only a few terms; iii) functions which involve infinite series, i.e like Eq.(2); such functions have been used in the studies quoted earlier [9, 10, 11].

2.1 Cylinder geometry

The most trivial equilibrium solutions to Eq.(1) are those with rotational symmetry, i.e. one-dimensional functions $\psi = \psi(R)$; several examples can be constructed. One two-dimensional solution has elliptic surfaces with constant ellipticity $E(> 0)$ [4]

$$\psi(R, Z) = \psi_0\, x^2\ ,\ x^2\ =\ (R/R_0 - 1)^2 + Z^2/(R_0^2\, E^2)\ ,\ J_Z(\psi) = -\frac{\psi_0}{\mu_0 R_0^2}(2 + 2/E^2) \quad (13)$$

This solution is purely of academic interest. The solution to Eq.(3) for the orthogonal function χ is easily found

$$\tan\chi\ =\ \frac{(Z/R_0)^{E^2}}{(R/R_0) - 1} \quad (14)$$

The solution has four fold symmetry w.r.t the R and Z axes ($\chi = 0, \pi/2, \pi, 3\pi/2$).

2.2 Toroidal equilibria without separatrix

One simple solution in toroidal geometry with flux surfaces ressembling ellipses is

$$\psi(R, Z) = \psi_0\, x^4\ ,\ x^4\ =\ (R^2/R_0^2 - 1)^2 + Z^2/(R_0^2 E^2)\ ,\ J_\phi(\psi) = -\frac{\psi_0}{\mu_0 R_0^2}(\frac{2}{RE^2} + \frac{8R}{R_0^2}) \quad (15)$$

Again the ellipticity E must be positive to obtain closed ψ surfaces. The ψ derivatives in J_ϕ are constant

$$\frac{dp}{d\psi}\ =\ -\frac{8\psi_0}{\mu_0 R_0^4}\ ,\ f\frac{df}{d\psi}\ =\ -\frac{2\psi_0}{R_0^2 E^2} \quad (16)$$

The solution to Eq.(3) for the orthogonal function χ is again easily found

$$\tan\chi\ =\ \frac{(Z/R_0)^{4E^2}}{(R/R_0)^2 - 1} \quad (17)$$

The solution in Eq.(15) is again mainly of academic interest. The solution (15) has up-down symmetry. Four curves ($\chi = 0, \pi/2, \pi, 3\pi/2$) are straight lines. Another toroidal equilibrium solution, also of academic interest, as it cannot be established experimentally, is the degenerate solution found by Palumbo [42] and Bishop & Taylor [43]. The degeneracy of this solution arises from B being constant on each flux surface. This solution is a toroidal mimimum B equilibrium as found earlier [42]; it has B increasing and p decreasing away from the magnetic axis, i.e. the ideal confinement system in which guiding centre drift surfaces and flux surfaces coincide.

3 Solovev equilibrium

3.1 Solutions for $\psi, \boldsymbol{B}, \boldsymbol{J}$

An example of a compact analytic solution to Eqs.(1-3) is the Solovev equilibrium solution [3]. This solution has been used to analyse the stability of D-shaped JET configurations [44]; it has also been used extensively in Monte Carlo simulations [45, 46]. The solution describes seven classes of topologically different equilibria (see subsection 3.3 and Table I) and it is expressed by the equation

$$\psi(R,Z) = \psi_0\, x^4\ ,\quad x^4\ =\ (R^2/R_0^2-1)^2 + \frac{Z^2}{R_0^4\ E^2}(R^2\ -\ R_x^2) \tag{18}$$

The Solovev solution is up-down symmetric and does not contain the $R^2 log R$ term of the solution considered in [8]. If that term is added to Eq.(18) then the resulting solution has the undesirable property that the vertical field $B_Z \rightarrow \infty$ as $R \rightarrow 0$. None of the solutions (13,15,18) are truly global solutions, since the poloidal field B_{pol} does not fall off as $x^{-\gamma}, \gamma > 0$. They can thus only be made to represent a plasma equilibrium for x marginally larger than the separatrix value x_x. The ψ derivatives of Eq.(1), which are constant just as those of Eqs.(6,8), are given by

$$\frac{dp}{d\psi}\ =\ -\psi_0\ \frac{(8+2/E^2)}{\mu_0 R_0^4}\ ,\ f\frac{df}{d\psi}\ =\ 2\psi_0\ \frac{R_x^2}{E^2\ R_0^4} \tag{19}$$

The poloidal and toroidal magnetic field components are given by

$$\begin{aligned} B_R &= -\psi_0\ \frac{2Z(R^2-R_x^2)}{RR_0^4E^2} \\ B_\phi &= \frac{1}{R}\ [R_0^2\ B_{\phi 0}^2 + \frac{4}{E^2\ R_0^4}R_x^2\ \psi_0\ \psi]^{1/2} \\ B_Z &= \psi_0\ [\frac{4}{R_0^2}(\frac{R^2}{R_0^2}-1) + \frac{2Z^2}{R_0^4E^2}] \end{aligned} \tag{20}$$

The vacuum field on axis $B_{\phi 0}$ must be specified separately from ψ_0 in such a way as to make the safety factor on axis, $q_\psi(x=0) \approx 1$. The poloidal and toroidal current components are given by, respectively,

$$\begin{aligned} J_R &= -\frac{\psi_0 R_x^2}{\mu_0 R_0^4 E^2\ RB_\phi}\ B_R \\ J_\phi &= \frac{\psi_0}{\mu_0 R_0^4}\ [-\frac{8E^2+2}{E^2}R + \frac{4R_x^2}{RE^2}] \\ J_Z &= \frac{\psi_0 R_x^2}{\mu_0 R_0^4 E^2\ RB_\phi}\ B_Z \end{aligned} \tag{21}$$

Equation(21) shows us that $\mathbf{J}\times\mathbf{B} \sim [-B_Z, 0, B_R]$, i.e. axisymmetry. Although the ψ surfaces resemble those of experimentally produced tokamak equilibria, e.g. like those of JET, neither the poloidal magnetic field components (Eq.19), nor the poloidal current components (Eq.20) can be said to correspond to experimental conditions.

3.2 Parameters and separatrix

The parameter R_0 denotes the magnetic axis and R_x denotes the position of a separatrix (see below). Both are determined by a set of four separate parameters (R_1, R_2, R_m, Z_m) which define a D-shaped reference surface going through the three points $(R_1, 0), (R_2, 0), (R_m, Z_m)$. These four coordinates are used to define the parameters of Eq.(18) as follows [3]:

$$a = \frac{R_2 - R_1}{2},\ R_0^2 = \frac{R_1^2 + R_2^2}{2},\ R_x^2 = \frac{R_1^2 R_2^2 - R_{\rm m}^4}{R_1^2 + R_2^2 - 2R_m^2},\ E^2 = \frac{Z_{\rm m}^2}{R_1^2 + R_2^2 - 2R_m^2} \tag{22}$$

We note that both $R_x^2 < 0$ and $E^2 < 0$ allow for solutions (see Table I). The reference surface passing through the four points $(R_1, 0)$, $(R_2, 0)$, $(R_m, \pm Z_m)$ can be thought of as the plasma boundary, when a plasma limiter is present. The boundary value is

$$\psi_b = \psi_0\, x_b^4\ ,\quad x_b^4\ =\ (R_2^2 - R_1^2)^2\ /\ (4R_0^4) \tag{23}$$

A separatrix exists except when $R_m = R_0$; the separatrix has the ψ value

$$\psi_x = \psi_0\, x_x^4\ ,\ x_x^4\ =\ (R_0^2 - R_x^2)^2 / R_0^4 \tag{24}$$

The separatrix consists of two curves, a vertical line and a curve, which can be an ellipse, a hyperbola or a straight line as shown in Figures 1-7 and in Table I

$$R = R_x\ \ ,\ \ R^2 + \frac{Z^2}{E^2} = 2R_0^2\ -\ R_x^2 \tag{25}$$

When $2R_0^2 = R_x^2$ the separatrix curve degenerates to a straight line as the RHS of Eq.(25) vanishes; this line and the vertical line together form a triangle. The vertical line and curve intersect at the X-point (R_x, Z_x). The elliptic separatrix intersects the R and Z axes at $(R_s, 0), (0, Z_s)$ respectively. These coordinates are given by

$$R_x\ =\ R_x\ ,\ Z_x^2\ =\ E^2\ (2R_0^2 - 2R_x^2)\ ,\ R_s^2\ =\ 2R_0^2 - R_x^2\ ,\ Z_s^2\ =\ E^2\ (2R_0^2 - R_x^2) \tag{26}$$

3.3 7 classes of equilibria

There are seven classes of topologically different equilibria possible as shown in Table I; the equilibria have plasma surfaces, i.e. surfaces with $0\ <\ \psi\ <\ \psi_x$, which show D-shapes or inverted D-shapes. The seven classes are distinguished by the value of R_m relative to the values of (R_1, R_2), as shown in Table I which lists the R_m range for each class. The seven classes have positive/negative R_χ^2, E^2 etc. as indicated. In classes 3 and 4 there is no separatrix. These various choices permit a variety of geometries as can be seen from Figures 1 to 7. These figures show contours of constant ψ, i.e. flux surfaces for a given value of R_m which is also given in Table I. The separatrix curves in Figures 1-2 and 5-7 are shown as dot-dash curves. Figures 1-7 also show the orthogonal contours of constant χ (see Eqs.3,33). Subsection 3.5 describes how χ is computed. The stability of equilibria of classes 1 to 7 has been examined in reference [44] as a benchmark for the then future JET tokamak. Only classes 1 and 2 were found to exhibit stability, the remaining classes

being mainly of academic interest. The class 1 equilibria have been used in extensive Monte Carlo guiding-centre drift calculations of the ion thermal heat flux [45] and self consistent test particle modelling of a plasma [46]. From Eqs.(19,21) we can see that class 2 equilibria, which approximate spherical tokamak equilibria, are degenerate as they have no poloidal current density, $J_R = J_Z = 0$ and the toroidal field is a pure vacuum field $B_\phi = R_0/RB_{\phi 0}$ as $f' = 0$. The flux function ψ of Eq.(18) can be positive, zero or negative as shown in Table I. The contour with $\psi = 0$ lying outside the separatrix is given by

$$Z^2(R, \psi = 0) \;=\; E^2 \, \frac{(R^2 - R_0^2)^2}{R_x^2 - R^2} \tag{27}$$

but does not exist for classes 2, 3, and 4. At the origin $\psi(R = 0, Z = 0) = \psi_0$ for all classes, while on the magnetic axis $\psi(R_0, 0) = 0$. For class 4 equilibria both $R_x \to \infty$ and $E^2 \to \infty$ such that Eq.(18) takes the form $x^4 = (R^2/R_0^2 - 1)^2 + cZ^2$, where $c = R_x^2/E^2 = (R_1^4 + R_2^4)/(2Z_m^4)$. This expression for c enters Eqs.(18-21) for class 4 equilibria.

3.4 Flux surface profiles

The flux surface profiles are functions of x only. The first profile we show is the Shafranov shift function. It is expressed in terms of the dimensionless flux surface label x in Eq.(5)

$$\Delta(x) \;=\; 1/2R_0 \, \left[(1 + x^2)^{1/2} \;+\; (1 - x^2)^{1/2}\right] \;-\; 1/2(R_1 + R_2) \tag{28}$$

where the first bracketed term is the centre of flux surface x and the second term is the centre of the boundary flux surface x_b. The maximum value occurs on axis $x = 0$

$$\Delta(0) \;=\; 1/2(R_1^2 + R_2^2)^{1/2} \;-\; 1/2(R_1 + R_2) \tag{29}$$

The f function of Eq.(19) can be integrated

$$f(x) \;=\; RB_\phi \;=\; (R_0^2 \, B_{\phi 0}^2 + \frac{4}{E^2 \, R_0^4} R_x^2 \, \psi_0 \, \psi)^{1/2} \tag{30}$$

As already noted $f_0 = R_0 B_{\phi 0}$ needs to be specified. The pressure derivative (Eq.19) can also be integrated. The integration is made w.r.t. the flux surface label x

$$p(x) = \frac{\psi_0^2}{\mu_0 R_0^4} \;\; (8 + \frac{2}{E^2})(x_b^4 - x^4) + p_b \tag{31}$$

in which p_b denotes an edge (or pedestal) pressure which also needs to be specified. Notice that it is possible to normalise x in Eq.(5) such that the boundary value becomes $x_b = 1$ instead of that given by Eq.(23).

3.5 ψ, x and χ curves

The flux surfaces for all seven classes are expressed by the equation

$$Z(R, x) \;=\; \pm \; \left[E^2 R_0^4 \, \frac{x^4 \;-\; (R^2/R_0^2 - 1)^2}{R^2 - R_X^2}\right]^{1/2} \tag{32}$$

The $\pm$ in Eq.(32) imply symmetry w.r.t. the $Z = 0$ axis (up-down symmetry). The gradients are found from Eq.(18)

$$\begin{aligned}\nabla x^4 &= [\frac{4R}{R_0^2}(R^2/R_0^2 - 1) + \frac{2}{R_0^4 E^2} Z^2 R,\ 0\ , \frac{2}{R_0^4 E^2} Z(R^2 - R_x^2)] \\ \nabla\chi &= \xi^{-1}(R,Z)\ [-\frac{2}{R_0^4 E^2} Z(R^2 - R_x^2),\ 0\ , \frac{4R}{R_0^2}(R^2/R_0^2 - 1) + \frac{2}{R_0^4 E^2} Z^2 R] \end{aligned} \quad (33)$$

where $\xi(R,Z)$ can be any continuous function (see Eq.3). Equation(4) can now be written as a highly non-linear differential equation

$$(\frac{\partial Z}{\partial R})^{\chi} = -\frac{Z(R^2 - R_x^2)}{2E^2 R(R^2 - R_0^2)\ +\ Z^2 R} \quad (34)$$

We have not found the general solution $\chi(R,Z)$ to Eqs.(3,33) with ψ given by Eq.(18). We have only found a solution for the special case of class 2 with $R_x = 0$

$$\tan\chi\ =\ \frac{(Z/R_0)^{4E^2}}{(R/R_0)^2 - 1 + (Z/R_0)^2\ (2E^2 - 1)^{-1}} \quad (35)$$

The constant χ curves for the special case of class 2 equilibria are given by

$$R(Z,\chi)\ =\ R(-Z,\chi)\ =\ R_0\ \left[1 + (\frac{Z}{R_0})^{4E^2}\cot\chi - (\frac{Z}{R_0})^2(2E^2 - 1)^{-1}\right]^{1/2} \quad (36)$$

i.e. these curves also have up-down symmetry w.r.t. $Z = 0$. We notice from Eq.(36) that $R(Z = 0,\chi) = R_0$ and $\partial R/\partial Z(Z = 0,\chi) = 0$. This shows that all χ curves join the vertical line $R = R_0$ at the magnetic axis $(R_0, 0)$, i.e. a cusp geometry. The function ξ in Eq.(33) corresponding to the solution (35) is

$$\xi^{-1}(R,Z)\ =\ \frac{Z^{4E^2} E^2}{R\ [(R^2 - R_0^2 + Z^2/(2E^2 - 1))^2 + Z^{8E^2}]} \quad (37)$$

i.e. ξ is a non-trivial function. We notice from Eq.(37) that ξ cannot be factorized in to separate functions of R and Z as assumed in [13]. The dashed curves in Figures 1-7 are those of constant χ and show the same cusp geometry as the solution Eq.(36). For the class 1 equilibrium of Figure 1 the origin $(R,Z) = (0,0)$ shows a second cusp geometry. For classes 1, 2 and 5-7 the χ curves feature an x-point which coincides with the x-point (R_x, Z_x) (see Eq.26), since at the x-point both gradients vanish ($\nabla\psi = \nabla\chi = 0$). The two curves which we can label χ_x go through the x-point and separate (R,Z) space into four regions, just as the separatrix curves separate the ψ curves into four regions. The two χ_x curves are not shown in Figures 1,2 and 5-7 as they are difficult to compute by our χ tracking algorithm. This algorithm starts from Eq.(33) with the unknown function ξ being equal to 1 on a selected surface $x = x_b$ (see Eq.(23)). We refer to x_b as the plasma boundary; in the case of JET this surface would be the boundary in a L-mode limiter plasma, the limiter being at R=4 [m]. A discrete set of points on x_b with a uniform distribution in the geometric angle θ is selected. A standard predictor-corrector scheme is used first to integrate Eq.(33) from the boundary x_b to the axis $x = 0$; secondly we start again from the boundary x_b and integrate outwards towards the edge of the calculation region. Such a computational procedure is necessary because of the cusp geometry of the magnetic axis. Some χ contours in Figures 1, 2, 6 and 7 have not been computed.

4 Topology of ψ and χ curves

In the previous sections we were looking at specific equilibrium solutions. In this section we shall examine some topological properties of general equilibria. This work is a continuation of the work in [4]. It has been motivated by attempts to reconstruct equilibria with the minimum amount of information and assumptions.

4.1 Coordinate transformations and metrics

In this section we shall be concerned with the transformations from the axi-symmetric (R, ϕ, Z) geometry to that of (ψ, ϕ, χ), ϕ being the ignorable coordinate. The metrics and the Jacobian of the transformation are given by textbook expressions

$$\begin{aligned} h_\psi^{-2} &= \mid \nabla\psi \mid^2 \ , \ h_\chi^{-2} = \mid \nabla\chi \mid^2 \ , \ h_\psi^2 = R_\psi^2 + Z_\psi^2 \ , \ h_\phi^2 = R^2 \ , \ h_\chi^2 = R_\chi^2 + Z_\chi^2 \\ \tau &= h_\psi \, h_\chi \ , \ \xi = \frac{h_\chi}{h_\psi} \ , \ \sqrt{g} = h_\psi \, h_\phi \, h_\chi = R \, (R_\psi Z_\chi - R_\chi Z_\psi) \end{aligned} \tag{38}$$

Subscripts ψ imply differentiation w.r.t. ψ etc. The derivatives are linked via the two dimensional Jacobian τ or via the ratio of metrics ξ as

$$\begin{aligned} R_\psi &= \tau \, \chi_Z \ , \ Z_\psi = -\tau \, \chi_R \ , \ R_\chi = -\tau \, \psi_Z \ , \ Z_\chi = \tau \, \psi_R \\ R_\psi &= \xi^{-1} \, Z_\chi \ , \ Z_\psi = -\xi^{-1} \, R_\chi \ , \ \psi_R = \xi \, \chi_Z \ , \ \psi_Z = -\xi \, \chi_R \end{aligned} \tag{39}$$

Various other relations can be worked out. By differentiation of the derivatives above we can derive two elliptic equations

$$\frac{\partial}{\partial R}(\xi \, \frac{\partial \chi}{\partial R}) + \frac{\partial}{\partial Z}(\xi \, \frac{\partial \chi}{\partial Z}) = 0 \ , \ \frac{\partial}{\partial R}(\xi^{-1} \, \frac{\partial \psi}{\partial R}) + \frac{\partial}{\partial Z}(\xi^{-1} \, \frac{\partial \psi}{\partial Z}) = 0 \tag{40}$$

Equation(40) has been used in the work by Vabishchevich et al. [47] on the variable-inversion formulation of MHD equilibria. The Grad-Shafranov equation can now be expressed in terms of either the metrics (h_ψ, R, h_χ) or the function ξ of Eq.(3)

$$\frac{R}{h_\psi h_\chi} \, \frac{\partial}{\partial \psi}(\frac{h_\chi}{R h_\psi}) = \mid \nabla\psi \mid^2 \frac{R}{\xi} \frac{\partial}{\partial \psi}(\frac{\xi}{R}) = -\mu_0 R^2 p' - f f' \tag{41}$$

Our work has involved examining the variations with χ of this equation on a curve of constant ψ. In particular we have attempted to establish a link between the extrema for $\nabla\psi, \nabla\chi$ and the extrema for the curvatures of the ψ and χ curves.

4.2 Curvature

The curvature of one single curve $\psi = \psi_1(\chi)$, i.e. a flux surface, is expressed from either the parametric curve representation $R = R(\psi_1, \chi), Z = Z(\psi_1, \chi)$ or from $Z = Z(\psi_1, R)$ by

textbook expressions which involve first and second derivatives w.r.t χ or R

$$\kappa_\psi = \frac{R_\chi Z_{\chi\chi} - Z_\chi R_{\chi\chi}}{(R_\chi{}^2 + Z_\chi{}^2)^{3/2}} \ , \quad [R_\chi = \frac{\partial R}{\partial \chi} \ etc.]$$
$$\kappa_\psi = \frac{Z_{RR}}{(1 + Z_R^2)^{3/2}} \ , \quad [Z_R = (\frac{\partial Z}{\partial R})_{\psi_1} \ \text{etc.}] \tag{42}$$

where the subscript ψ_1 implies that the derivative is at constant ψ. The curvature of one single curve $\chi = \chi_1(\psi)$ is similarly derived from either the curve representation $R = R(\psi, \chi_1)$, $Z = Z(\psi, \chi_1)$ or from $R = R(\chi_1, Z)$

$$\kappa_\chi = \frac{R_\psi Z_{\psi\psi} - Z_\psi R_{\psi\psi}}{(R_\psi{}^2 + Z_\psi{}^2)^{3/2}} \ , \quad [R_\psi = \frac{\partial R}{\partial \psi} \ etc.]$$
$$\kappa_\chi = \frac{R_{ZZ}}{(1 + R_Z^2)^{3/2}} \ , \quad [R_Z = (\frac{\partial R}{\partial Z})_{\chi_1} \ \text{etc.}] \tag{43}$$

The χ curves are the streamlines for the guiding centre drift flow orthogonal to the flux surfaces (see next section).

4.3 Formulae for Solovev class 2 equilibria

The derivatives required to calculate Eqs.(50-51) can be derived from Eqs.(32,36). By straightforward differentiation we get some rather lengthy expressions so we introduce the normalised variables $y = R/R_0), z = Z/R_0$ and $e = (2E^2 - 1)^{-1}$ in order to compress these expressions. We then get

$$(R_Z)_{\chi_1} = \frac{2E^2 z^{4E^2-1} \cot\chi_1 - ez}{1 + z^{4E^2} \cot \chi_1 - ez^2}$$
$$(Z_R)_{\psi_1} = \frac{x_1^4 + y^4 - 1}{[x_1^4 - (y^2-1)^2)^{1/2} \, y^2} \tag{44}$$

where from Eq.(18) $x_1^4 = \psi_1$. The second derivatives involve lengthier expressions

$$(R_{ZZ})_{\chi_1} = \frac{[2E^2(4E^2-1)z^{4E^2-2} \cot\chi_1 - e][1 + z^{4E^2} \cot\chi_1 - ez^2][2E^2 z^{4E^2-1} \cot\chi_1 - ez]^2}{[1 + z^{4E^2} \cot\chi_1 - ez^2]^{3/2}}$$
$$(Z_{RR})_{\psi_1} = -\frac{4y^4[x_1^4 - (y^2-1)^2] + 2[(y^2-1)(2y^2-1) - x_1^4][x_1^4 - y^4 + 1]}{y^3[x_1^4 - (y^2-1)^2]^{3/2}} \tag{45}$$

Insertion of Eqs.(44-45) into Eqs.(42-43) yield very lengthy expressions from which the curvatures can be computed.

5 The Cauchy problem

The starting point in our study is as follows: we assume that some curve Γ_b, e.g. the plasma boundary, but not necessarily so, is specified either as an analytic function $\Gamma_b(\chi) = \Gamma_b(R, Z)$

or as a set of N_χ discrete coordinates $\Gamma_b(R_j, Z_j), j = 1, N_\chi$. On Γ_b we assume that both ψ and $\nabla\psi$ are given, i.e. we are given both Dirichlet and Neuman boundary conditions for ψ. Both ψ and $\nabla\psi$ may be given either as analytic functions or as a set of discrete numerical values. The discrete case corresponds to the result from the fast plasma boundary identification of the intershot analysis as described in section 1.4 and in references [34]-[37]. Furthermore the plasma current density $J_\phi = 0$ outside the boundary. The problem to be solved is known as the Cauchy problem: can two one-dimensional functions $(p(\psi), f(\psi))$ (see Eqs.(6-8)) be determined from the knowledge of two different one-dimensional functions $\psi(\chi)$ and $\nabla\psi(\chi)$ as well as the geometric shape of the curve Γ_b external to the plasma. In the next three subsections we outline the three step procedure which was originally intended as the method of solution.

5.1 Step 1: advance geometry (R, Z) to surfaces $\psi \pm \delta\psi_0$

We start by inwards-outwards integration from ψ_b to $\psi_b \pm \delta\psi_0$), where $\delta\psi_0$ is subscripted 0 to indicate that it is an infinitesimally small constant; this integration immediately yields two new ψ surfaces known either analytically or from the coordinates of N_χ discrete points. The infinitesimal spatial displacements $\boldsymbol{\delta}_\pm = (\delta R, \delta Z)_\pm$ to the inside (subscript -) and outside (subscript +) ψ surfaces from an arbitrary point (ψ_b, χ) on Γ_b are found from the equation

$$(\delta R_\pm, \delta Z_\pm) = \lim_{\delta\psi_0 \to 0} \pm \frac{\delta\psi_0}{\mid \nabla\psi \mid^2} \left(\frac{\partial\psi}{\partial R}, \frac{\partial\psi}{\partial Z}\right) \tag{46}$$

By applying this equation to all points on Γ_b we have made use of all the given data. The above equation expresses the gradients on the + and - sides of Γ_b and it is the result of the limiting process (Taylor expansion)

$$\mid \nabla\psi \mid_\pm = \lim_{\delta\psi_0 \to 0} \frac{\delta\psi_0}{\mid \boldsymbol{\delta}_\pm \mid} \tag{47}$$

The displacements are parallel to the vector $\nabla\psi$, i.e. along curves of constant χ. Equation(46) can always be solved except for the special case of an x-point on a separatrix at which $\nabla\psi = 0$; in this case the Taylor expansion must be made to second order, but that requires specification of $\nabla^2\psi$ which is not included in the data. In all other cases the Taylor expansion has yielded the (R, Z) geometry of three ψ surfaces with values $\psi = (\psi_b - \delta\psi_0, \psi_b, \psi_b + \delta\psi_0)$.

5.2 Step 2: test functional form of $\Delta_*\psi$

We now know the geometry of three ψ surfaces $\psi = (\psi_b - \delta\psi_0, \psi_b, \psi_b + \delta\psi_0)$ and the variation of $\nabla\psi$ on one surface. This knowledge could possibly enable us to test whether Eq.(1) holds for the given data on the boundary $\psi = \psi_b$. This test is similar, but not identical to that used in reference [4] in which it was assumed that (R, Z) geometries of all ψ surfaces are given. The operation on the three surfaces must yield results which are expressed in the

following three forms, of which it is the second we shall have to solve for

$$\begin{aligned}
\Delta_*\psi(\psi &= \psi_b - \delta\psi_0) &&= \pi(\psi_b - \delta\psi_0)\ R^2 \ +\ \phi(\psi_b - \delta\psi_0) \\
\Delta_*\psi(\psi &= \psi_b) &&= \pi(\psi_b)\ R^2 \ +\ \phi(\psi_b) \\
\Delta_*\psi(\psi &= \psi_b + \delta\psi_0) &&= 0
\end{aligned} \tag{48}$$

where π and ϕ have been used to represent the values of p' and ff' on the surfaces $\psi = \psi_b$ and $\psi = \psi_b - \delta\psi_0$ as indicated, i.e. π and ϕ are constant on each ψ surface. The surface just outside the plasma boundary Γ_b has zero current density. The determination of the two constants π and ϕ on Γ_b can be made from just two points, i.e. only two values of χ on Γ_b are required. The test on the data thus becomes: can Eq.(48) be satisfied at all points on Γ_b? Only if this is the case will the data represent an equilibrium solution to Eq.(1). In practice and with inexact (experimental) boundary data, $\pi(\psi_b)$ and $\phi(\psi_b)$ must be determined from the average $< \Delta_*\psi(\psi = \psi_b) >$ over the surface Γ_b, either analytically or from N_χ discrete points. Our work on the test of Eq.(48) has involved relating $\Delta_*\psi$ to the curvatures given by Eqs.(42-43). We emphasize that this work is *incomplete.*

5.3 Step 3: advance $\nabla\psi$ to surfaces $\psi \pm \delta\psi_0$

Once the two numbers $\pi(\psi_b)$ and $\phi(\psi_b)$ have been determined we know the rate of change of $\nabla\psi$ on Γ_b as it is expressed by Eq.(48). This should allow us to calculate $\nabla\psi$ on the surfaces $\psi \pm \delta\psi_0$ from the Taylor expansion

$$\nabla\psi(\psi = \psi_b \pm \delta\psi_0) \ \approx\ \nabla\psi(\psi = \psi_b) \ \pm\ \Delta_*\psi \ \mid \boldsymbol{\delta}_\pm \mid \tag{49}$$

By repeating the sequence of Eqs.(46-49) we could advance the solution to the surfaces $\psi \pm 2\delta\psi_0$ and so on until the magnetic axis would have been reached. The end point of our study would thus have been to determine not only the solution $\psi(R, Z)$ to Eq.(1), but in the process the components $p'(\psi)$ and $f(\psi)f'(\psi)$ of Eq.(1) would also have been determined, without the specification of their particular functional form, such as the examples of Eqs.(6-8).

6 Guiding centre velocities

The guiding centre drift velocity $\mathbf{u}$ is described in the article by Sivukhin [48]. The equations derived in that article are based upon the standard guiding centre formalism, also outlined in the article, which puts constraints on the spatial and temporal variations of the magnetic field. The guiding centre drift velocity includes four components

$$\mathbf{u} = \mathbf{u}_\parallel + \mathbf{u}_\nabla + \mathbf{u}_\kappa + \mathbf{u}_\mathbf{E} \tag{50}$$

These four components are known to represent respectively the parallel, the ∇B, the curvature and $\mathbf{E} \times \mathbf{B}$ drifts. The drift motions are expressed in terms of the parallel particle velocity $v_\parallel$, the particle parallel and perpendicular energies $E_\parallel$ and $E_\perp$, the particle charge

Ze, the unit vector $\mathbf{b} = \mathbf{B}/B$, the curvature vector $\kappa = (\mathbf{b}\cdot\nabla)\mathbf{b}$ and the electric field vector $\mathbf{E}$. The latter should not be confused with the particle energy $E = mv^2/2$. The drift components are expressed to first order in $\nabla\mathbf{b}$ following the general expansion in [48]

$$\mathbf{u}_{\|} = [v_{\|} + (E_{\perp}/(ZeB))\ \mathbf{b}\cdot\nabla\times\mathbf{b}]\ \mathbf{b} \tag{51}$$

$$\mathbf{u}_{\nabla} = (E_{\perp}/(ZeB))\ (\mathbf{b}\times\nabla B)/B \tag{52}$$

$$\mathbf{u}_{\kappa} = (2E_{\|}/(ZeB))\ \ \mathbf{b}\times\kappa \tag{53}$$

$$\mathbf{u}_{\mathbf{E}} = \mathbf{E}\times\mathbf{B}\ /\ B^2 \tag{54}$$

In order to see how the first three components compare we insert the equilibrium field Eq.(20) and its derivatives (not presented here) into Eqs.(38-41). Lengthy expressions arise and to shorten these we retain only the leading terms by assuming that $B_{\phi}/B \equiv 1$, ie $B_{\phi} \gg B_R, B_z$. One term is $O(1)$ (vertical drift) and the other terms are $O(\rho_i/R)$. The Larmor radius is $\rho_i = mv_{\perp}/eB$ as Z=1 is assumed; the cosine of the pitch angle is $\xi = v_{\|}/v$. We then get

$$\begin{aligned}
u_R &\simeq v[\xi + \frac{\rho_i}{R}2\frac{B_Z}{B}\ \xi^2 + \frac{\rho_i}{R}\frac{B_R}{B}\frac{\psi_0 R_x^2}{R_0^4 B}(1-\xi^2)]\ \frac{B_R}{B} \\
u_{\phi} &\simeq v[\xi - \frac{\rho_i}{R}\frac{B_Z}{B}(1-3\xi^2)]\ \frac{B_{\phi}}{B} \\
u_Z &\simeq v[\xi\frac{B_Z}{B} + \frac{\rho_i}{R}(1+\xi^2)]
\end{aligned} \tag{55}$$

From these useful, but approximate, expressions we can evaluate the drift velocity component orthogonal to the flux surfaces which is given by

$$u_x \ \ = \ \ \boldsymbol{u}\ \cdot\ \boldsymbol{\nabla}\psi\ /\ |\ \boldsymbol{\nabla}\psi\ | \tag{56}$$

We insert Eq.(50) and get

$$u_x(R,Z)\ \simeq\ v\ \frac{\rho_i\ B_R}{R\ B_{pol}}[-(1+\xi^2)\ +\ \frac{B_Z^2}{B^2}\xi^2] \tag{57}$$

where B_{pol} is the poloidal field. The equation shows us that u_x is far from being constant on a flux surface x and that $u_x \geq 0$ for $Z \geq 0$ and $u_x \leq 0$ for $Z \leq 0$, i.e. the dominant drift is the vertical drift. Both terms in the square bracket will contribute to the ion thermal flux as evaluated in reference [45], since they contain ξ to even powers, assuming that the particle (ion) distribution function $f_i(\xi)$ is roughly independent of ξ; because $B_Z \ll B$ the second term is negligible compared with the first term. In Figures 8 and 9 we show contours of constant u_x in the (R,Z) plane for a class 1 equilibrium (Figure 8) and a class 2 equilibrium (Figure 9). For both figures we have set $\xi = 0.5, E = E_{\perp} + E_{\|} = 1[keV]$ as an example. Only the upper half-plane is shown as $u_x(R,Z) = -u_x(R,-Z)$ for an up-down symmetric equilibrium. The contours, which qualitatively look the same for all values of (ξ, E), are superimposed on the separatrix curves which are shown as dash-dot curves. For both Figures 8 and 9 the u_x contours show a banana shaped region, the dashed curve, in which u_x is at maximum; this banana shaped region is tilted inwards for D-shaped equilibria; for the inverse D-shapes shown in Figures 5-7 the banana shaped region will tilt outwards. On each plasma surface x the ion heat flux q_i due to collisions and guiding centre drifts, as described in [45, 46], is therefore peaked where the surface x intersects this banana shaped

regions, since $q_i \sim u_x$. The banana shaped region thus represents a "guiding centre drift loss cone" through which the neoclassical heat loss is at maximum. This loss cone surrounds the locus of inflexion points for the χ curves, i.e. those points where $\kappa_\chi = 0$ (Eq.43). The maximum cross field drift thus occurs where the streamlines (the χ curves) are straight rather than curved.

7 Conclusion

We have described the nature of a problem in equilibrium reconstruction which we have regarded as a natural progression from the early work [4]. We have emphasized in the introduction that this problem remains unresolved.

ACKNOWLEDGEMENT

The present work was jointly funded by United Kingdom Engineering and Physical Sciences Research Council and by the European Communities under the contract of association between EURATOM and UKAEA. The views and opinions expressed in this paper do not necessarily reflect those of the European Commission.

References

[1] Morozov, A.L., Solovev, L.S., Reviews of Plasma Physics, Vol.2, Consultants Bureau, New York (1966).

[2] Solovev, L.S., Shafranov, V.D., Reviews of Plasma Physics, Vol.5, Consultants Bureau, New York (1966).

[3] Solovev, L.S., Zh. Ehksp. Teor. Fiz. **53** (1967) 626. (Sov. Phys. J.E.T.P. **26** (1968) 400).

[4] Christiansen, J.P., Taylor, J. B., Nucl. Fusion **22** (1982) 111.

[5] Shafranov, V.D., Zh. Ehksp. Teor. Fiz. **33** (1957) 710. (Sov. Phys. J.E.T.P. **6** (1958) 545).

[6] Grad, H., Proc. of the Second United Nations Conference on the Peaceful Uses of Atomic Energy, United Nations, Geneva, **31** (1958) 190.

[7] Lüst, R., Schlüter, A., Zeitschrift für Naturforschung **12A** (1957) 850.

[8] Zheng, S.B. et al., Phys. of Plasmas **3** (1996) 1176.

[9] Pfirsch, D., Rebhan, E., Nucl. Fusion **14** (1974) 547.

[10] Hernegger, F., Maschke, E.K., Nucl. Fusion **14** (1974) 119.

[11] Mazzucato, E., Phys. Fluids **18** (1975) 536.

[12] Barfield, W.D., J. Comp. Phys. **5** (1969) 23.

[13] Potter, D.E., Tuttle, G.H., J. Comp. Phys. **13** (1973) 483.

[14] Christiansen, J.P., et al., "Global energy confinement H-mode database for ITER", Nucl. Fusion **32** (1992) 291.

[15] Lackner, K., Proc. 2nd European Conf. on Computational Physics, Garching, North Holland Publishing Company (1976) 33.

[16] Field, J.J., Papaloizou, J.C.B., J. Plasma Physics **18** (1977) 347.

[17] McNamara, B., Methods of Computational Physics **16**, Academic Press (1976) 211.

[18] Callen, J.D., Dory, R.A., Phys. Fluids **15** (1972) 1523.

[19] Thomas C.Ll., Culham Laboratory Report CLM-P339 (1973).

[20] Feneberg, W., Lackner, K., Nucl. Fusion **13** (1973) 549.

[21] Zakharov, L.E., Nucl. Fusion **13** (1973) 595.

[22] Chu, M.S., Dobrott, D., Jensen, T.H., Phys. Fluids **17** (1974) 1183.

[23] Lao, L.L., Hirshman, S.P., Wieland, R.M., Phys Fluids **24(B)** (1981) 1431.

[24] Lao, L.L. et al., Comp. Phys. Comm., **27** (1982) 129.

[25] Lao, L.L., Comp. Phys. Comm., **31** (1984) 201.

[26] Goldston, R.J., J. Comp. Phys. **43** (1981) 61.

[27] Hawryluk, R.J., An empirical approach to tokamak transport (Proc. Course and Workshop, Varenna, 1979). Vol. **1**, CEC, Brussels (1980) 19.

[28] Attenberger, S.E., Houlberg, W.A., Hirshman, S.P., J. Comp. Phys. **72** (1987) 435

[29] Taroni, A., JET Report JET-IR(88)03 (1988).

[30] Asp, E. et al., PPCF **47** (2005) 505.

[31] Taroni, A. Springman, E. JET Report JET-R(86)03 (1986).

[32] Lao, L.L. et al., Nucl. Fusion **25** (1985) 1611.

[33] Shafranov, V.D., Plasma Physics **13** (1971)757.

[34] Swain, D.W., Neilson, G.H., Nucl. Fusion **22** (1982) 1015.

[35] Feneberg, W., Lackner, K., Martin, P., Comp. Phys. Comm. **31** (1984) 143.

[36] Christiansen, J.P., J. Comp. Phys. **73** (1987) 85.

[37] Ellis, J.J. et al., Proceedings of IAEA Technical Meeting on magnetic diagnostics, Kharkov, Ukraine, Oct. 1994.

[38] O'Brien, D. et al., Nucl. Fusion **32** (1992) 1351.

[39] Appel, L. et al., in Controlled Fusion and Plasma Physics (Proc. 21st Eur. Conf. Rome, 2006), Vol. 1 ***B***, Part II, European Physical Society, Geneva (2006) 648.

[40] Blum, J., Le Foll, J., Thooris, B., Comp. Phys. Comm. **24** (1981) 235.

[41] Blum, J. et al., Nucl. Fusion, **30** (1990) 1475.

[42] Palumbo, D., Il Nuovo Cimento X **53B** (1968) 507.

[43] Bishop, C.M., Taylor, J.B., Phys. Fluids **29** (1986) 1144.

[44] Green, B.J., Zehrfeld, H.P., Nucl. Fusion **17** (1977) 1133.

[45] Christiansen, J.P., Connor, J.W., Plasma Phys. and Contr. Fusion **46** (2004) 1537.

[46] Christiansen, J.P., Connor, J.W., Plasma Phys. and Contr. Fusion **48** (2006) 1551.

[47] Vabishchevich, P.N., et al., Sov. J. Plasma Phys. **4** (1978) 554.

[48] Sivukhin, R., Reviews of Plasma Physics, Vol.1, Consultants Bureau, New York (1965).

Class	$\mathbf{R_m}$**range**	$\mathbf{R_m^2}$**[m^2]**	$\mathbf{R_x^2}$	$\mathbf{E^2}$	ψ	**Separatrix**
1	$R_1^2 < R_m^2 < R_1 R_2$	7	2.5	0.51	$\pm$	Ellipse
2	$R_1 R_2 = R_m^2$	8	0	0.7656	+	Ellipse
3	$R_1 R_2 < R_m^2 < R_0^2$	9	-	1.53	+	None
4	$R_m^2 = R_0^2$	10	∞	∞	+	None
5	$R_0^2 < R_m^2 < R_1^2 + R_2^2 - R_1 R_2$	11	28.5	-1.53	$\pm$	Hyperbola
6	$R_m^2 = R_1^2 + R_2^2 - R_1 R_2$	12	$2R_0^2$	-0.7656	$\pm$	Triangle
7	$R_1^2 + R_2^2 - R_1 R_2 < R_m^2 < R_2^2$	14	16.5	-0.3828	$\pm$	Hyperbola

Table I. The seven classes of topologically different equilibria of the Solovev type [3]. The chosen values of R_m^2 have been chosen for Figures 1-7 and correspond to $R_1 = 2$ [m], $R_2 = 4$ [m], $Z_m = 1.75$ [m] and $\psi_0 = 0.76225$ [Vs], $B_{\phi 0} = 1.0$ [T]. These values are typical for 1MA JET equilibria, whose edge safety factor is in the range $3 < q_\psi(x = x_b) < 4$. The configuration parameters for the class 1 equilibrium used in the Monte Carlo calculations [45, 46] are as follows. The maximum Shafranov shift (see Eq.(29)) becomes $\Delta(0) = 10^{1/2} - 3 = 0.16$ [m]. The plasma cross section is $A = 5.46$ [m^2], the plasma surface is $S = 161$ [m^2] and the plasma volume is $V = 99.7$ [m^3]. The plasma beta poloidal is $\beta_I = 0.91$ and corresponds to a plasma energy $W = 1.5\ 10^6$ [J].

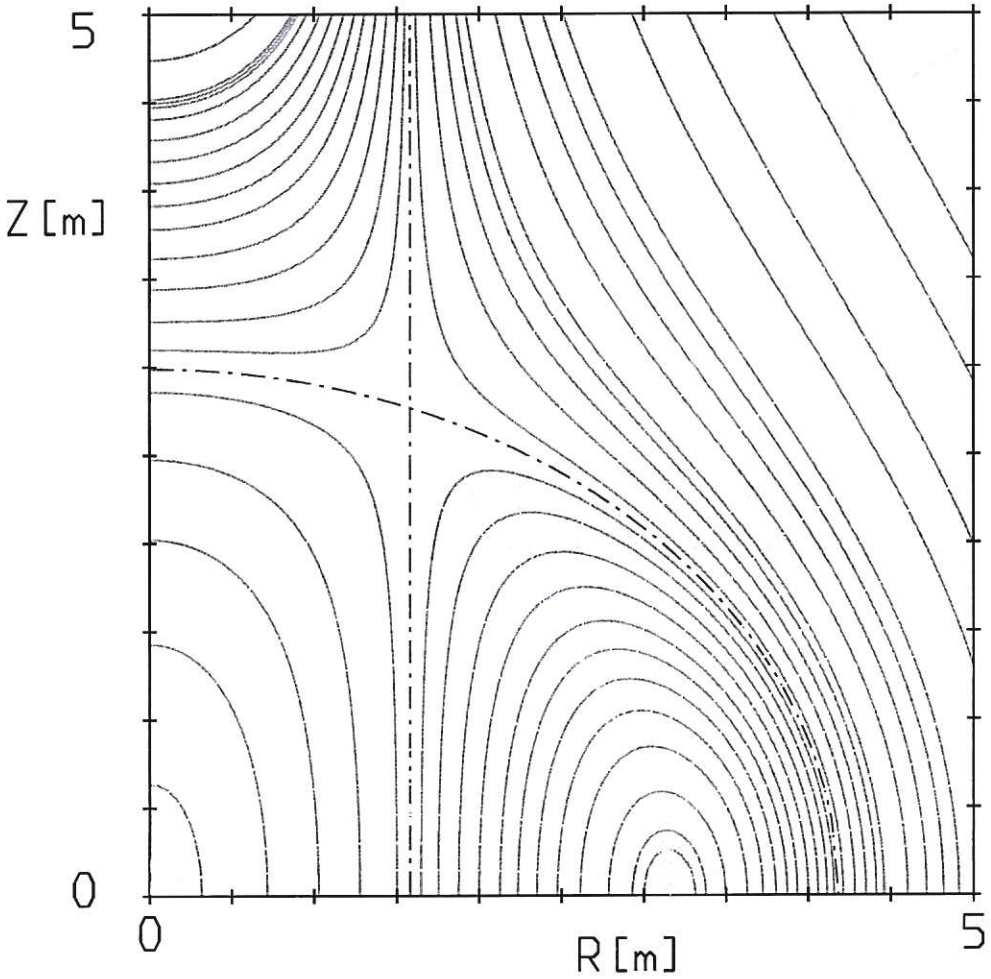

Figure 1: Flux surfaces of the Solovev equilibrium [3] of class 1 (see Table I). It shows a separatrix comprising a straight line at $R = R_x < R_0$ and an ellipse (dot-dash curves) forming a D-shape. The surfaces with constant values of ψ are shown in real (R, Z) space together with the orthogonal contours of constant χ (see Eqs.3,33). The equilibrium configuration corresponds to JET geometry as explained in Table I. Figures 2-7 show contours of constant ψ and χ for the remaining equilibrium classes.

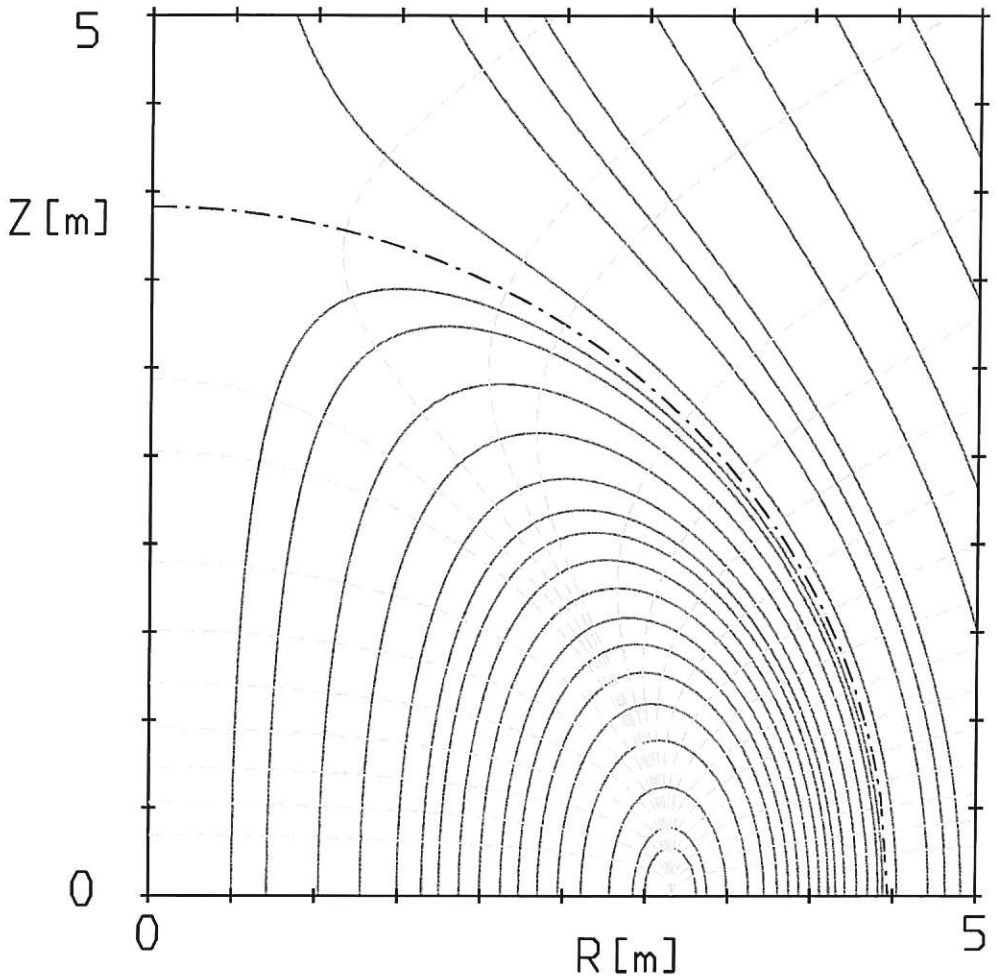

Figure 2: The Solovev equilibrium of class 2 with the separatrix coinciding with Z axis $R_x = 0$, i.e. an approximation to a spherical tokamak. This equilibrium configuration is however degenerate, as it has no poloidal current density $J_R = J_Z = 0$ and the toroidal field is a vacuum field $B_\phi = R_0/RB_{\phi 0}$.

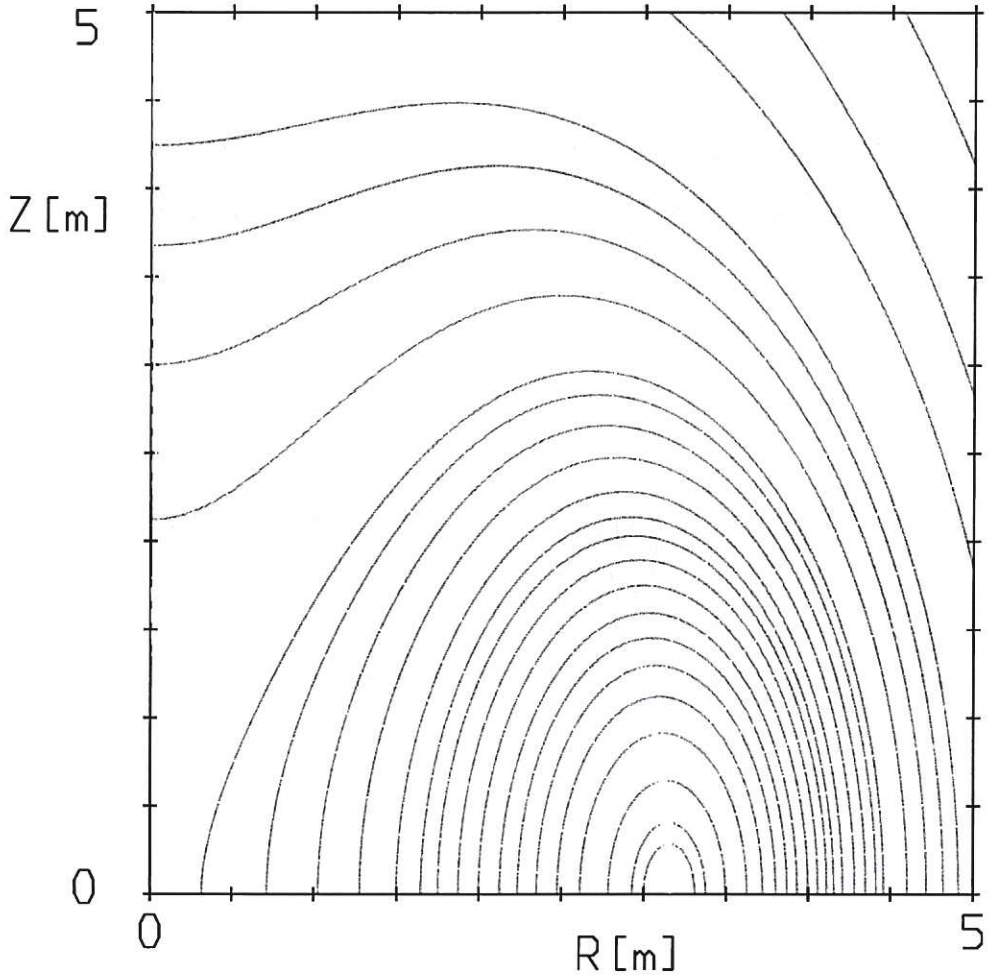

Figure 3: The Solovev equilibrium of class 3 has no separatrix.

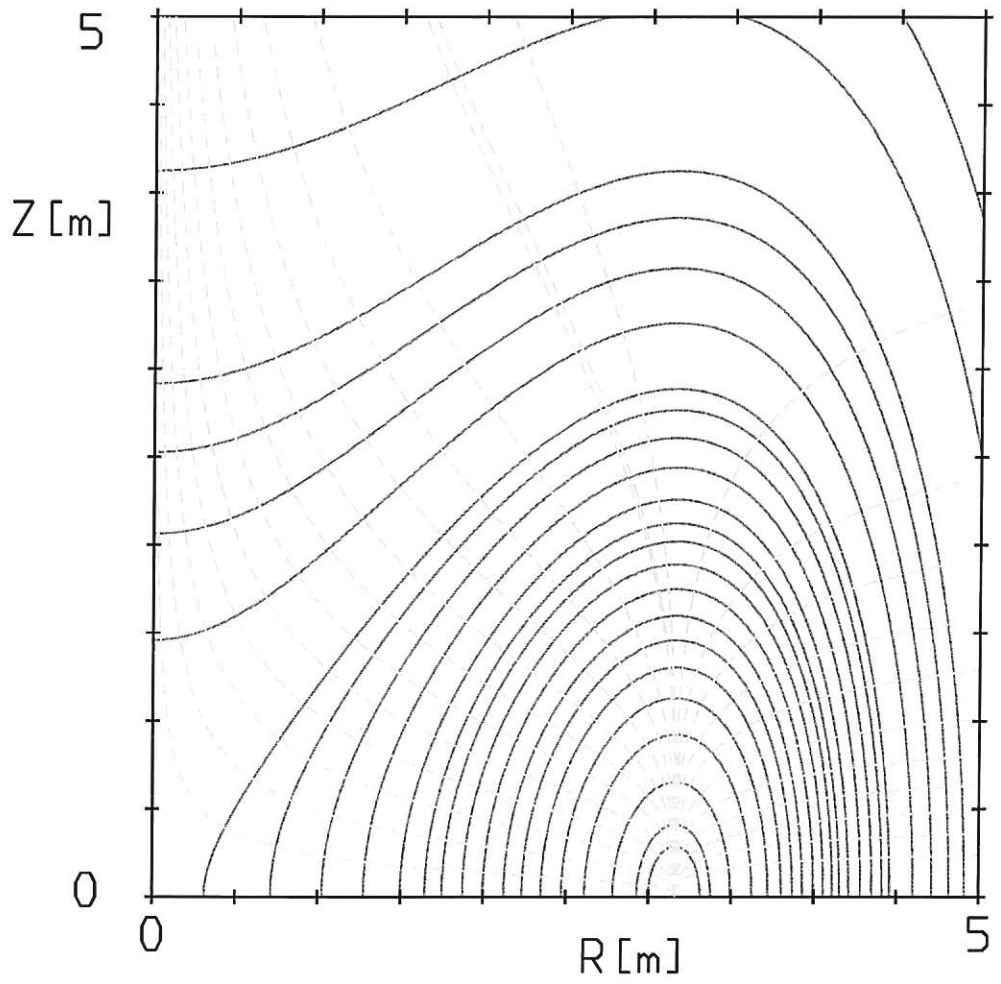

Figure 4: The Solovev equilibrium of class 4 with the separatrix location at $R_x \to \infty$.

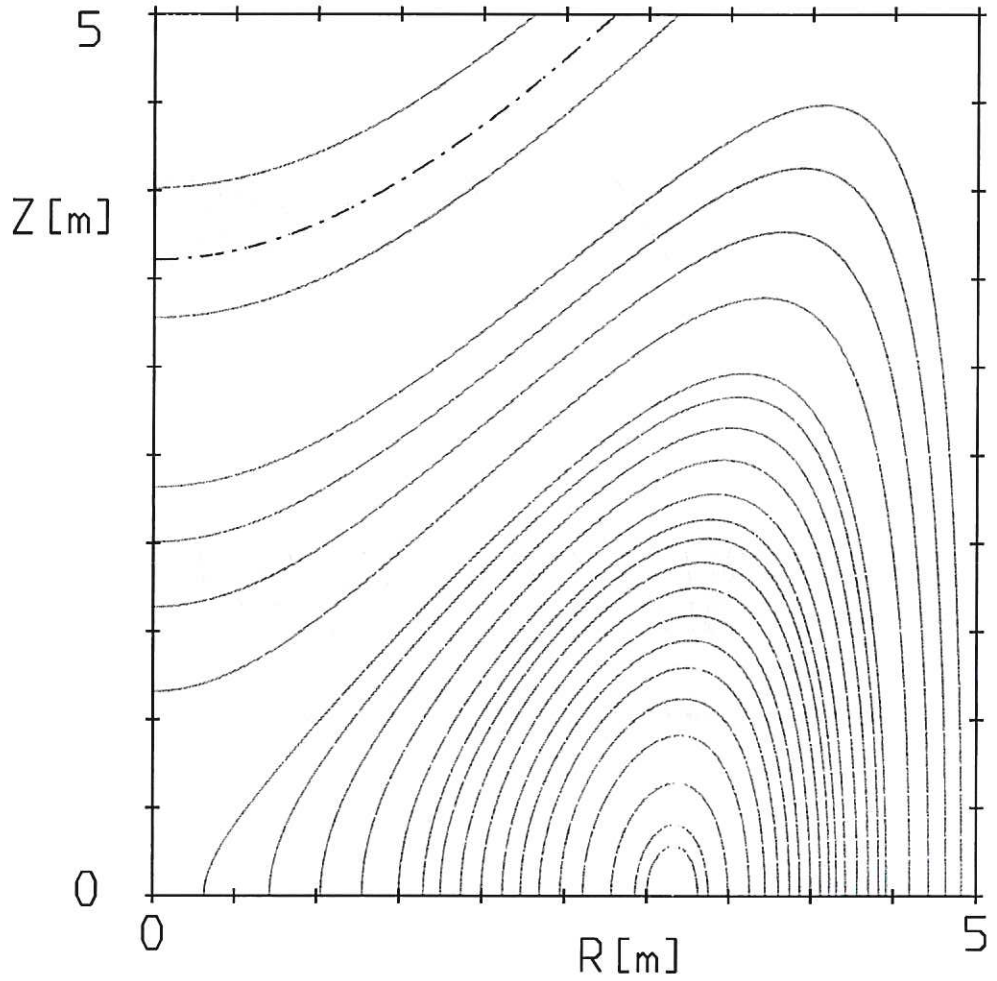

Figure 5: The Solovev equilibrium of class 5 has a separatrix (dot-dash curves) consisting of a straight line $R_x > R_0$ which is not shown as it lies beyond $R = 5$m. The "vertical" hyperbola is shown a the dot-dash curve.

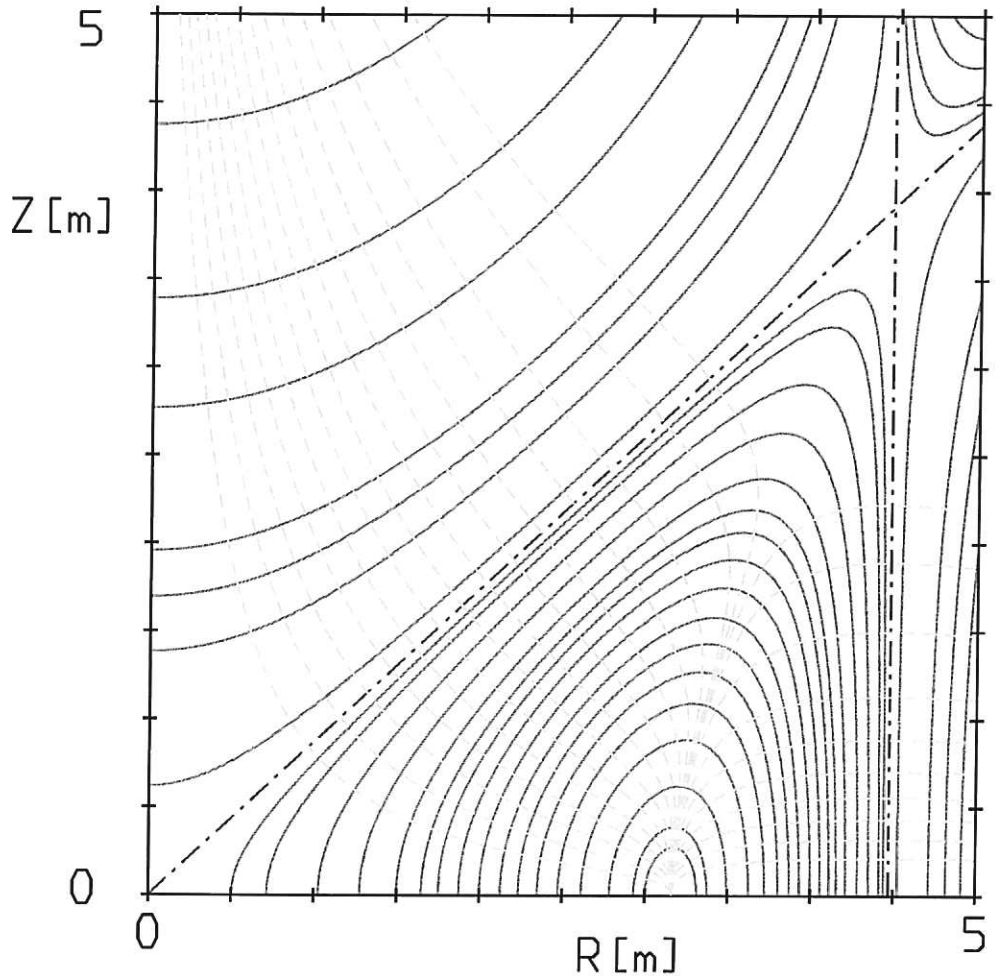

Figure 6: The Solovev equilibrium of class 6 has a separatrix (dot-dash lines) consisting of two intersecting lines. This triangular plasma equilibrium is of academic interest only.

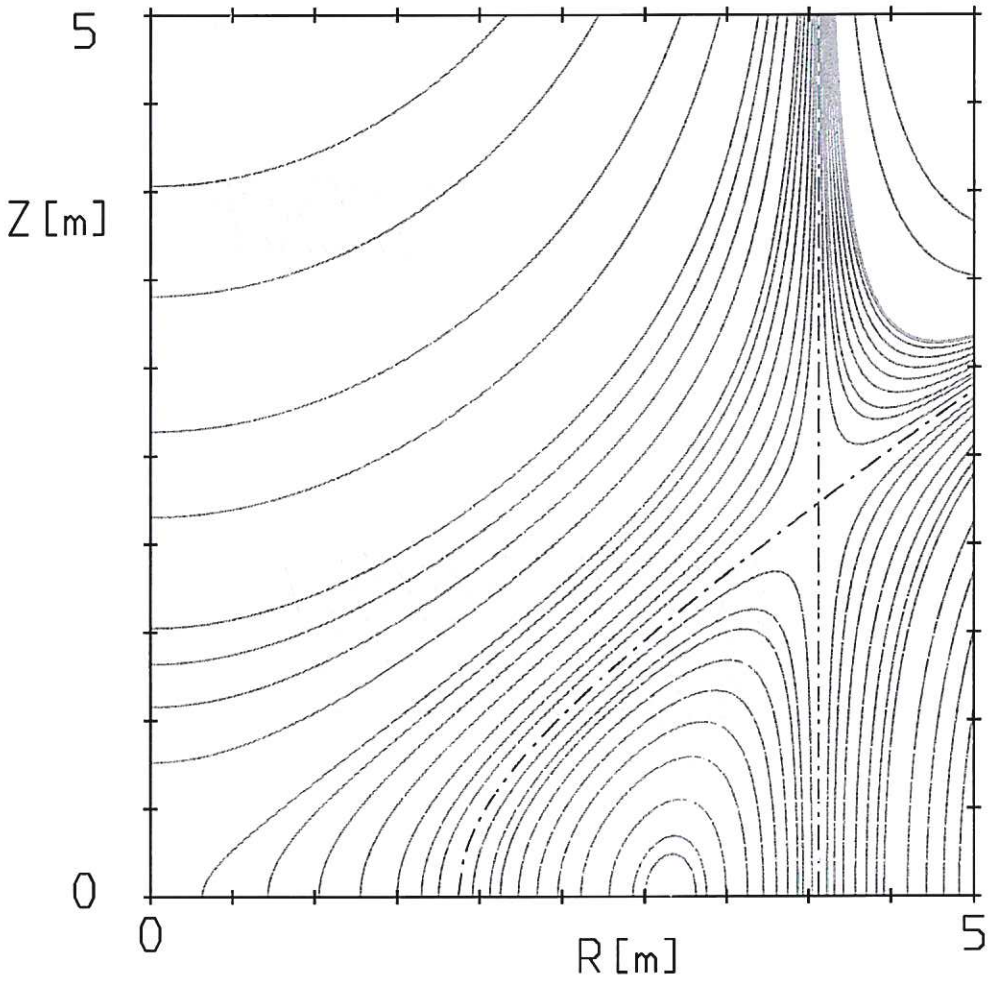

Figure 7: The Solovev equilibrium of class 7 has a separatrix consisting of a straight line $R_x > R_0$ and a "horizontal" hyperbola both shown as dot-dash curves. It is of the inverse D–shape type equilibrium.

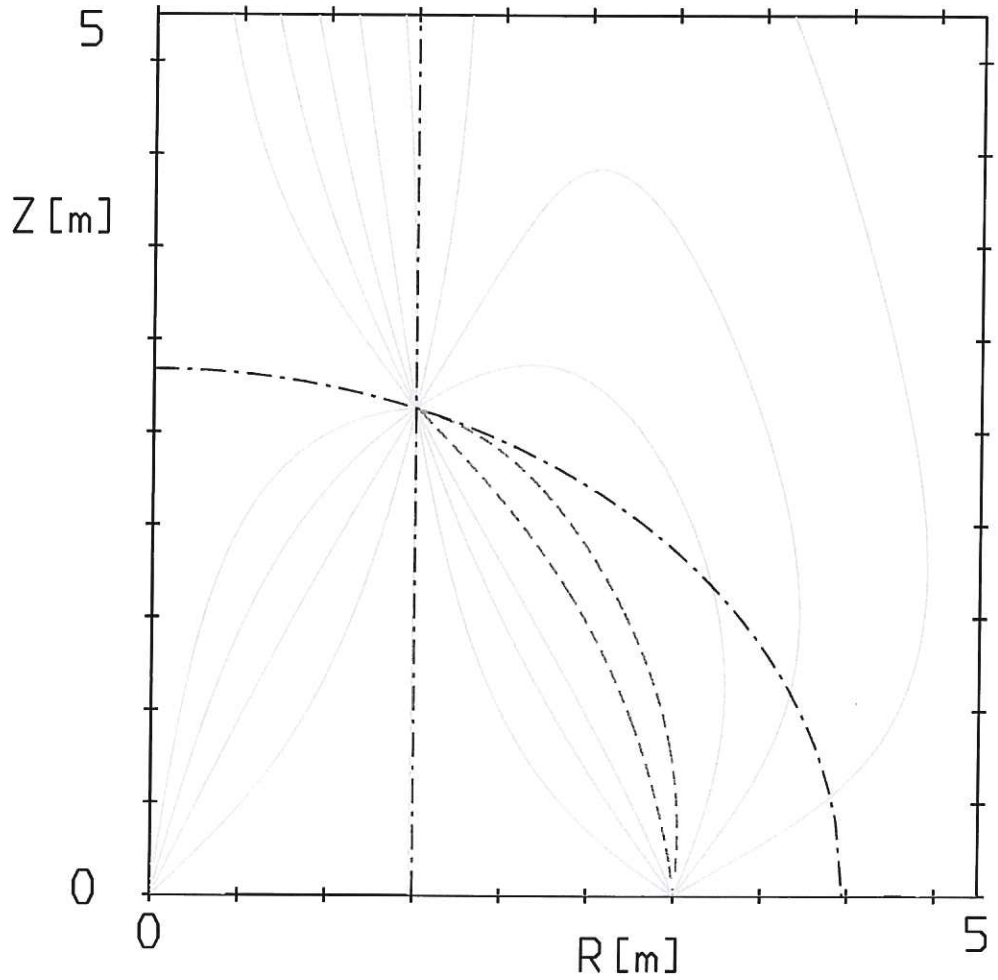

Figure 8: Contours of the guiding centre drift velocity u_x orthogonal to the flux surfaces for class 1 equilibria. The contours reveal a banana shaped "loss cone" like region where u_x is at maximum. This region is shown by the dashed curve.

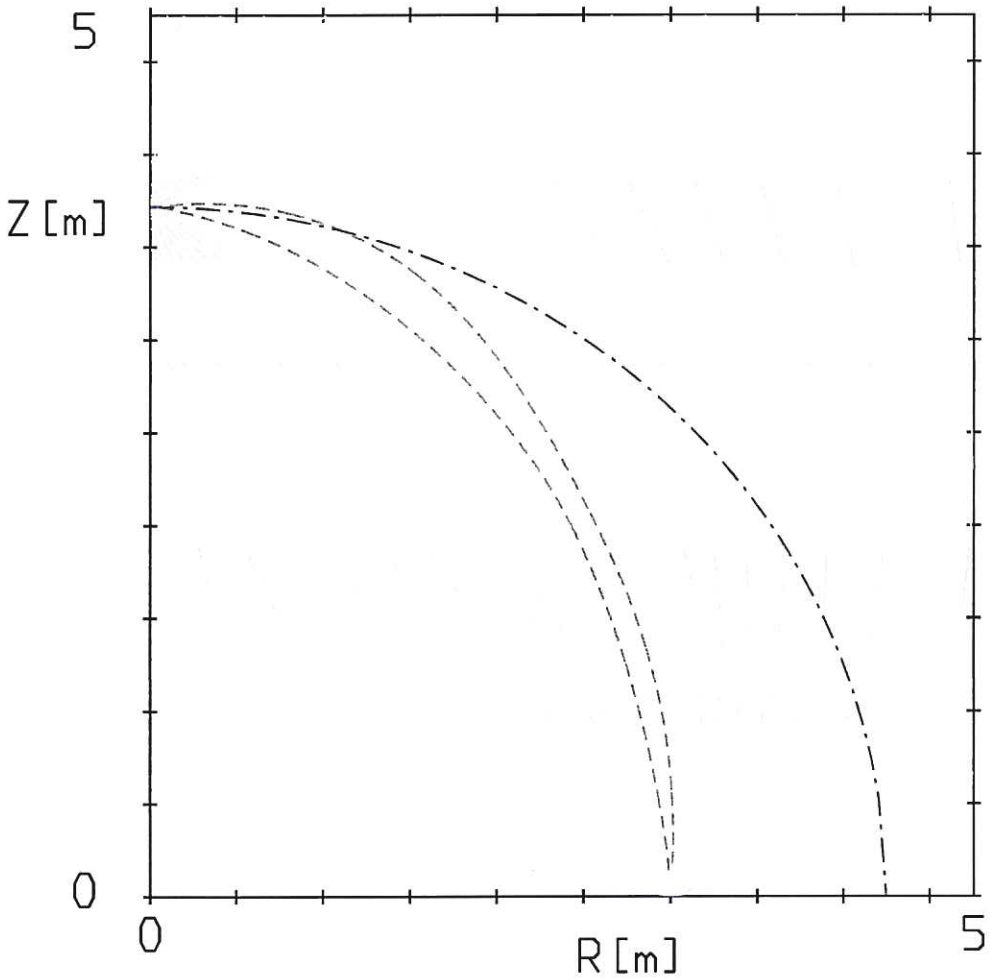

Figure 9: Contours of the guiding centre drift velocity u_x orthogonal to the flux surfaces for class 2 equilibria. The region shown by the dashed curve represents, as in Figure 8, a banana shaped "loss cone" like region where u_x is at maximum.